Published in final edited form as:
Nanomedicine. 2012 November ; 8(8): 1355–1363. doi:10.1016/j.nano.2012.02.005.

In vivo particle tracking and photothermal ablation using plasmon-resonant gold nanostars

Hsiangkuo Yuan, MD[a], **Christopher G. Khoury, MS**[a], **Christy M. Wilson, PhD**[b], **Gerald A. Grant, MD**[b], **Adam J. Bennett, BSE**[a], and **Tuan Vo-Dinh, PhD**[a,c,d,*]

[a]Department of Biomedical Engineering, Duke University, Durham, NC, USA

[b]Department of Surgery, Division of Neurosurgery, Duke University Medical Center, Durham, NC, USA

[c]Department of Chemistry, Duke University, Durham, NC, USA

[d]Fitzpatrick Institute for Photonics, Duke University, Durham, NC, USA

Abstract

Gold nanostars offer unique plasmon properties that efficiently transduce photon energy into heat for photothermal therapy. Nanostars, with their small core size and multiple long thin branches, exhibit high absorption cross-sections that are tunable in the near-infrared region with relatively low scattering effect, making them efficient photothermal transducers. Here, we demonstrate particle tracking and photothermal ablation both in vitro and in vivo. Using SKBR3 breast cancer cells incubated with bare nanostars, we observed photothermal ablation within 5 minutes of irradiation (980-nm continuous-wave laser, 15 W/cm^2). On a mouse injected systemically with PEGylated nanostars for 2 days, extravasation of nanostars was observed and localized photothermal ablation was demonstrated on a dorsal window chamber within 10 minutes of irradiation (785-nm continuous-wave laser, 1.1 W/cm^2). These preliminary results of plasmon-enhanced localized hyperthermia are encouraging and have illustrated the potential of gold nanostars as efficient photothermal agents in cancer therapy.

Keywords

Nanotechnology; Photothermal therapy; Simulation; Two-photon photoluminescence; Gold nanostars

Introduction

Aspherical gold nanoparticles (AuNPs) represent a new type of plasmonic-active system favorable for biological applications, particularly cancer therapy. AuNPs are generally nontoxic, small in size (<100 nm), and can be delivered selectively to the tumor site.[1–3] Because the plasmonic behavior of AuNPs is largely determined by their geometry and size, aspherical AuNPs typically exhibit plasmons in the near-infrared (NIR) region.[4,5] This region is called the "tissue therapeutic window" because of the lower optical attenuation from water and blood in this spectral range (650–900 nm).[6] At the plasmon resonance, the absorption cross-section of aspherical AuNPs is strongly enhanced to several orders of magnitude higher than an organic dye; aspherical AuNPs absorb NIR photoenergy strongly,

*Corresponding author: Department of Biomedical Engineering, Duke University, Box 90281, Durham, NC 27708, USA. tuan.vodinh@duke.edu (T. Vo-Dinh).

thereby efficiently transducing the incident light into heat.[2,7–9] Moreover, because of their unique plasmonic property, aspherical AuNPs emit strong two-photon photoluminescence (TPL), allowing direct particle visualization under multiphoton microscopy.[10–12] Combining a preferential tumor site accumulation, efficient NIR photothermal transduction, and particle optical traceability, aspherical AuNPs are ideal candidates for in vivo photothermal therapy (PTT).

Therapeutic hyperthermia has been used to treat cancer for many years. Elevating the temperature to >42°C kills malignant cells through apoptosis or necrosis.[13] To date, several PTT studies with plasmon-enhanced local tumor hyperthermia have been demonstrated using different classes of NIR-absorbing AuNPs, including silica-gold nanoshells, gold–gold sulfide nanoshells, nanorods, nanocages, hollow nanospheres, nanocubes, and branched nanoparticles.[2,5,7–9,14–20] AuNPs can passively or actively concentrate in the tumor region due to an enhanced permeability and retention (EPR) effect or specific biotargeting, respectively.[1,2,21] Aside from reticuloendothelial system clearance, extended serum half-life has been demonstrated on nanoparticles coated with poly(ethylene glycol) (PEG). Hirsch et al. first reported using PEGylated silica-gold nanoshells on breast cancer cells under 820-nm continuous-wave (CW) laser (35 W/cm^2 for 7 minutes in vitro or 4 W/cm^2 for 6 minutes in vivo) for localized hyperthermia.[22] Later, PTT was also demonstrated by Huang et al using nanorods labeled with antibodies to epidermal growth factor receptor in vitro (10 W/cm^2 for 4 minutes, 800-nm CW laser), and subsequently using PEGylated nanorods in vivo under lower irradiance (2 W/cm^2 for 10 minutes, 808-nm CW laser).[9,23] PTT using nanorods of different surface functionalization has been demonstrated by several groups.[15,16,19,20,24] PTT studies using newly developed aspherical nanoparticles have been reported in vitro using gold–gold sulfide nanoshells (80 W/cm^2 for 7 minutes, 808-nm CW laser),[18] nanocubes (4 W/cm^2 for 15 minutes, 532-nm CW laser),[17] immunotargeted nanocages (1.5 W/cm^2 for 5 minutes, 810-nm pulsed laser),[25] peptide-labeled hollow nanospheres (32 W/cm^2 for 3 minutes, 808-nm CW laser),[26] and HER2 antibody–labeled branched nanoparticles (38 W/cm^2 for 5 minutes, 690-nm CW laser).[14] In vivo application using PEGylated nanocages (0.7 W/cm^2 for 10 minutes, 808-nm CW laser) and PEGylated hollow nanospheres (0.5 W/cm^2 for 1 minutes, 808-nm CW laser) also showed promising results.[26,27] The laser irradiance used in the latter study was the closest to conforming to the maximum permissible exposure of skin (0.33 W/cm^2 for 808-nm CW laser) from the American National Standards Institute (ANSI) Laser Safety Standards.[28]

To be ideal as a PTT transducer, the nanoparticles should be biocompatible, simple in synthesis, small in size, plasmon-tunable in the NIR, and high in absorption to scattering cross-section ratio (C_{abs}/C_{sca}) for efficient photothermal transduction. At the moment, standard wet chemical nanoparticle syntheses are time-consuming, usually taking several hours to complete. Also, each class of nanoparticle employed has its own limitation. For example, synthesis of nanorods requires the use of cetyltrimethylammonium bromide (CTAB), which is potentially toxic to animals and human beings, and is difficult to replace for surface functionalization. Nanorods are also susceptible to reshaping under intense irradiation.[2] In the case of nanoshells, it can be challenging to achieve a uniform shell thickness.[9] For nanocages, although their C_{abs}/C_{sca} ratio is higher than nanorods and nanoshells,[4] the synthesis is elaborate, requiring titration with $HAuCl_4$ under 90°C monitored under ultraviolet-visible absorption.[9]

Over the last two decades, our laboratory has devoted extensive effort to develop metallic nanostructures for chemical and biological sensing.[29–31] Recently, we reported unique surface-enhanced Raman scattering–active nanoprobes based on star-shaped AuNPs (nanostars) nanoplatforms.[32,33] Nanostars, which contain multiple sharp branches with plasmons tunable in the NIR region, have gained wide interest in several biomedical arenas,

including surface-enhanced Raman scattering spectroscopy,[33–37] photoacoustic imaging,[38] biosensing,[39] photodynamic therapy,[33] PTT,[14] and magnetomotive imaging.[40] Although most nanostars synthesis requires the use of a surfactant (e.g., CTAB or polyvinylpyrrolidone), our group has fabricated surfactant-free nanostars that can be synthesized within 1 minute in high yield without the use of the toxic surfactant.[11] Unlike the branched nanoparticle (plasmon peaked at 635 nm) used previously for in vitro PTT,[14] our surfactant-free nanostars have plasmon peaks tunable in 650–950 nm,[11] which matches the tissue therapeutic window.[6] In addition, though metal nanoparticles are generally hard to visualize optically, nanostars generate efficient plasmon-enhanced TPL, offering a strong contrast under multiphoton microscopy for imaging and particle tracking both in vitro and in vivo.[11] With the simple synthesis, NIR plasmon tunability, and particle optical traceability, nanostars can be a new nanoplatform for PTT.

In this article we present, for the first time to our knowledge, in vitro and in vivo photothermal response validation using the surfactant-free gold nanostars we previously developed. Based on the simulation, their absorption dominates the total extinction at their plasmon peak, hence a high C_{abs}/C_{sca} ratio. Their biodistribution and photothermal response both in vitro (SKBR3 breast cancer cells) and in vivo (dorsal window chambers on mice) were investigated to illustrate nanostars' potential in PTT applications.

Methods

Synthesis and characterization of Gold Nanostars and Nanospheres

All chemicals were purchased from Sigma-Aldrich (St. Louis, Missouri) and used as received unless noted otherwise. Detailed surfactant-free nanostars synthesis and characterization has been presented elsewhere.[11] Briefly, citrate gold seeds were prepared by adding 15 mL of 1% (w/v) trisodium citrate to 100 mL of boiling $HAuCl_4$ (1 mM) under vigorous stirring for 15 minutes. The solution was cooled and filtered using a 0.22-μm nitrocellulose membrane. Gold nanostars (60 nm) were prepared using a seed-mediated method by quickly mixing $AgNO_3$ (100 μL, 3 mM) and ascorbic acid (50 μL, 0.1 M) together into 10 mL of $HAuCl_4$ (0.25 mM) containing HCl (100 μL, 1 M) and citrate gold seeds (100 μL, OD_{520} = 3.1), followed by filtration using a 0.22-μm nitrocellulose membrane. For 60-nm gold nanospheres synthesis, in 100 mL 0.25 mM boiling $HAuCl_4$ solution, 0.7 mL of 1% (w/v) trisodium citrate solution was added under vigorous stirring for 30 minutes. The solution was cooled and filtered using a 0.22-μm nitrocellulose membrane.

Bare (unlabeled) and PEGylated nanostars were prepared for this study. For bare nanostars, the solution underwent centrifugation wash (3500 g, 4°C) to concentrate the nanoparticles. For PEGylated nanoparticles, $SHPEG_{5000}$ (*O*-[2-(3-mercaptopropionylamino) ethyl]-*O*′-methylpolyethylene glycol, MW 5000) 5 μM was added immediately after the nanoparticle synthesis and mixed for 15 minutes, followed by 0.22-μm nitrocellulose membrane filtration and centrifugation wash (10,000 g, 4°C) to remove the unbound SHPEG and to concentrate the nanoparticles. Nanoparticles were examined by transmission electron microscopy (TEM; FEI Tecnai G^2 Twin, 200 kV; FEI, Hillsboro, Oregon) and visible-NIR spectroscopy (Shimadzu UV-3600; Shimadzu, Kyoto, Japan). The nanoparticles' hydrodynamic radius, zeta potential, and concentration were assessed by nanoparticle tracking analysis (NTA 2.1, NanoSight NS500; NanoSight Ltd., Wiltshire, United Kingdom).

Absorption and scattering cross-sections simulation

The three-dimensional (3D) nanostar simulations were performed using the Finite Element Method modeling software Comsol Multiphysics version 3.4 (Comsol Multiphysics,

Burlington, Massachusetts). Two 3D nanostar models were designed using the dimensions measured in our previous study.[11] The branches protrude in random direction but are normal to the core surface. The dielectric function of gold was modeled using the Lorentz-Drude model for gold,[41] and the surrounding water medium was set to a refractive index n of 1.33 to simulate nanostars in solution. The computational domain was bounded by a spherical perfectly matched layer to prevent any back-reflections onto the nanostar. The excitation source was a polarized incident plane wave E-field of unit amplitude with wavelength ranging from 300 nm to 1200 nm in 10-nm increments. The C_{abs} and C_{sca} were polarization-averaged by rotating the nanostar relative to the incident wavelength, to mimic nanostars' behavior in solution.

In vitro photothermal response validation

The SKBR3 breast cancer cells were cultured in McCoy 5A growth medium (10% v/v fetal bovine serum (FBS); Invitrogen, Carlsbad, California) in an incubator with a humidified atmosphere (5% CO_2) according to the American Type Culture Collection (Manassas, Virginia) protocol. Cells in exponential growth phase were used in experiments. The cells were seeded into 35-mm Petri dishes for more than 2 days until they had reached 80–90% confluency. Bare nanostars were washed, then resuspended and sonicated to 0.2 nM (measured by nanoparticle tracking analysis) in McCoy 5A immediately before use. Cells were incubated for 1 hour with 1 mL of bare nanostars in medium or medium alone, followed by phosphate buffered saline (PBS) washes and replacement with fresh medium. To assess intracellular particle distribution, cells were fixed in 4% (w/v) paraformaldehyde, stained with Hoechst 33342 (nuclear stain, 2 μg/mL in PBS; Invitrogen) and FM 1-43 FX (membrane stain, 4 μg/mL in PBS; Invitrogen) 30 minutes before imaging, then imaged under multiphoton microscopy (Olympus FV1000; Olympus America, Center Valley, Pennsylvania). For photothermal response validation, cell samples were kept on a 37°C heating stage and exposed to 980-nm diode laser irradiation (15 W/cm^2, spot size 8 mm^2) for 1, 3, and 5 minutes. Samples receiving medium alone but the same laser irradiation were used as controls. After 1 day, cells were examined by a live-cell staining procedure using fluorescein diacetate (1 μg/mL in PBS, incubated for 30 minutes) under a fluorescence microscope. Nonfluorescent fluorescein diacetate is converted to green fluorescent fluorescein by esterases in living cells.

In vivo photothermal response validation

Two female CD-1 nude mice were implanted with small dorsal window chambers 2 weeks before the photothermal experiment. During the treatment and imaging, anesthetized mice (intraperitoneal injection of ketamine/xylazine, 100/10 mg/kg) were placed on a heating frame to maintain body temperature at 37°C. On one mouse, PEGylated gold nanostars (50 nM, 50 μL in PBS, plasmon peak ~800 nm) were injected systemically through the retro-orbital vein and imaged via the dorsal window chamber under multiphoton microscopy. Another mouse injected with the same concentration of PEGylated gold nanospheres was used as a control. A bolus of fluorescein isothiocyanate (FITC)–dextran (250 kDa; 10 mg/kg body weight) was injected to visualize the vasculature when necessary. For photothermal response validation, a laser (785 nm CW, 1.1 W/cm^2, spot size 33.2 mm^2, 10 minutes) was applied on the third day (~48 hours after nanoparticle injection) to the center of the dorsal window chamber on both mice. The response was examined grossly and under multiphoton microscopy. All procedures were approved by the Duke University Institutional Animal Care and Use Committee.

Results

Nanostars synthesized by the procedure described above have sizes around 60 nm by TEM and showed star-shaped nanoparticles with ~8–10 protruding branches on a small 20- to 25-nm-diameter core (Figure 1, *inset*). Some branches even possess additional small branches. As shown in Figure 1, nanostars exhibit a broad plasmon spectrum, which peaks at 890 nm with an extinction coefficient of ~1×10^{10} M^{-1} cm^{-1} (calculated based on the plasmon peak intensity and particle concentration measured from the nanoparticle tracking analysis). A small peak at around 525 nm represents the plasmon of the core. The hydrodynamic size was 70 ± 32 nm, and the zeta potential was –31.3 mV. Upon the addition of serum-containing culturing media, the plasmon peak was red-shifted.

Figure 2 shows the simulated absorption and scattering cross-section spectra of nanostars of two different aspect ratios (ARs). The modeled nanostars show plasmon peaks at 810 nm and 960 nm with C_{abs}/C_{sca} ratios of 10.8 and 9.2, respectively (Table 1). The theoretical simulations indicate that nanostars not only predominantly absorb rather than scatter the incident photoenergy, but also have C_{abs}/C_{sca} ratios comparable to nanocages, higher than nanorods and nanoshells, and lower than Au-Au_2S nanoshells (Table 1).[4,18,25]

Before in vitro PTT experiments, the cellular uptake of bare nanostars (in FBS-containing growth medium) was investigated by multiphoton microscopy.[11] After 1 hour of incubation, bright white dots representing nanostars can be seen in cells incubated with nanostars (Figure 3, *A*, *B*) but not in cells treated with medium alone (Figure 3, *C*, *D*). Nanostars localized predominantly in the cytoplasm. Medium-treated cells showed only dye signals.

The photothermal response on SKBR3 cells receiving three different laser dosages (1, 3, 5 minutes) was examined using live-cell staining (Figure 4). Cancer cells were not visibly damaged after 1 minute (Figure 4, *A*) but were killed after 3 and 5 minutes (Figure 4, *B*, *C*) of irradiation. The photothermal response (i.e., the killing) was greater at minute 5 than at minute 3, reflecting a laser dose dependency. Cells without nanostars were fully viable (Figure 4, *D*, *E*) until after 5 minutes (Figure 4, *F*) of irradiation when they formed a small ablated region that was much smaller than with cells treated with nanostars and laser combined. Meanwhile, cells incubated with nanostars without irradiation showed no apparent death during the study period.

The photothermal response in vivo was examined through irradiating a small region (33.5 mm^2) on a dorsal window chamber of a mouse injected systemically with PEGylated nanostars (50 μL, 50 nM in PBS). Nanostars were PEGylated to reduce aggregation and extend serum half-life. Following the systemic injection of PEGylated nanostars, nanoparticles appeared mostly in the bloodstream during the first hour (Figure 5). After an hour, some nanostars stayed on the vessel wall (Supplementary Video S1, available online at http://www.nanomedjournal.com) or extravasated (Figure 5 *C*, *D*). After 48 hours, PEGylated nanostars distributed nonhomogeneously along the perivascular space and in tissue (Figure 6, *B*, *C*). Following 10 minutes of irradiation, a ring of blood oozing roughly the size of the laser spot was formed (Figure 6, *D*). The region was filled with nanostars and FITC-dextran leaked from the blood vessels (Figure 6, *E*, *F*), suggesting an effective photothermal ablation effect. Scarring can be seen 1 week after the laser irradiation on the backside of the window chamber. On gross inspection, a bluish discoloration of the spleen and liver on mice was seen, suggesting the clearance of nanoparticles by the reticuloendothelial system.[21]

Discussion

We demonstrated that nanostars can be an effective photothermal transducer both theoretically and experimentally. These nanostars offer several advantages. The surfactant-free synthesis of nanostars takes only minutes, which is a substantially simpler procedure than that required to form other classes of aspherical nanoparticles. The tunable, broad plasmon band of nanostars (Figure 1) allows fiexibility in the laser line matching compared to nanoparticles with narrow plasmon bands (e.g., nanospheres, nanorods). The successful photothermal ablation both in vitro (Figure 4) and in vivo (Figure 6) consequently validates the efficacy of nanostars for PTT.

From the simulation results, nanostars have a high C_{abs}/C_{sca} ratio (Figure 2 and Table 1). The tip-to-tip diameter is around 60 nm with a small core and thin branches. The overall volume is less than that of 60-nm nanospheres or nanoshells, hence there is less scattering. The presence of multiple branches on nanostars creates a structure that simulates an ensemble of multiple small rods, achieving comparable absorption but lower scattering than larger rods, and thus a high C_{abs}/C_{sca} ratio. Meanwhile, as size decreases, both C_{abs} and C_{sca} become smaller. At smaller size, the contribution of scattering to extinction becomes significantly less than that of absorption.[4,42] The Au-Au_2S nanoshells (25 nm) and nanocages (30 nm) are small, thus having smaller absolute C_{abs} and C_{sca} values. They possess higher C_{abs}/C_{sca} ratios but may require more particles to achieve the same degree of heating as their larger sized counterparts. In addition, Baffou et al noted that corners and sharp edges (e.g., branches) are favorable for heat generation.[43] More numerous sharp branches also produce a higher temperature factor in simulations.[44] With the presence of multiple sharp branches and the high C_{abs}/C_{sca} ratio, the nanostars could potentially heat more efficiently than nanospheres and rods.

The photothermal response relies on both the nanostars (plasmon position or intensity, particle concentration, C_{abs}/C_{sca} ratio) and laser (CW or pulsed, wavelength, irradiance, and duration). Although nanostars have high C_{abs}/C_{sca} ratio in simulation, the exact photothermal behavior needs to be investigated experimentally. To validate the photothermal response, nanostar heating in solution was first examined. Upon 5 minutes of laser irradiation (980 nm, 1.2 W), the temperature of 1 nM and 0.1 nM nanostar solutions increased to 80°C and 60°C, respectively, whereas nanospheres and deionized water only increased to near 40°C (Supplementary Figure S1, *B*). Without matching the nanospheres' plasmon to the laser line, temperature response from nanospheres is no different from that of deionized water at 980-nm irradiation. Meanwhile, when compared under the same plasmon intensity at the laser line (785 nm), nanorods displayed an identical response to similar-sized nanostars but required 2.5 times greater particle concentration (Supplementary Figure S1, *D*). The photothermal conversion efficiency of nanostars is probably greater than that of similar-sized nanospheres or rods. In vivo, after the laser irradiation (980 nm, 0.56 W/cm^2, 5 minutes), a similar finding showing a temperature rise to 45°C (with peripheral inflammation) was observed locally on a mouse receiving a subcutaneous injection of 0.6 pmol PEGylated nanostars but not PBS (Supplementary Figure S2). Although the laser wavelength used in the study caused some nonspecific water heating, the difference in temperature profile with and without nanostars clearly indicates efficient photothermal transduction.

The photothermal ablation using bare nanostars was demonstrated in vitro using SKBR3 breast cancer cells. The cellular uptake of nanoparticles is determined by their size, surface charge, shape, as well as any protein adsorbed on their surface.[2,45,46] The nanostars in growth medium were taken up by cells nonspecifically, possibly through endocytosis, and then localized predominantly in the cytoplasm (Figure 3, *A*, *B*).[47] Nonspecific cellular

uptake of nanostars showed a dependence on concentration (Supplementary Figure S3, *A*, *B*). Similar to previous studies on PEGylated nanoparticles,[12,46] PEGylated nanostars incubated with nonstarved cells exhibited minimal cellular uptake after 1 hour incubation (Supplementary Figure S3, *C*) and therefore were not used for the in vitro photothermal validation. Meanwhile, we observed mild aggregation (plasmon red-shifted) on bare nanostars when treated with FBS-containing growth medium (Figure 1). In contrast, bare nanostars are susceptible to complete aggregation under FBS-free growth medium and hence cannot be used. Passive adsorption of serum proteins onto the nanoparticle surface possibly protects the nanoparticles from severe aggregation upon exposure to various salts in the growth medium.[48] It is possible that nonspecific interaction between serum proteins and the cell membrane may facilitate the uptake of nanostars.[49,50] Although nanostars were slightly aggregated in FBS-containing growth medium, nanoparticle clustering may also facilitate their uptake.[45]

When applying localized irradiation to cells incubated with nanostars, a confined region of killing can be observed within 3 minutes (Figure 4, *B*). Laser irradiation alone generated no significant killing effect (Figure 4, *D*–*F*). With higher laser dosage, the photothermalablation effect becomes more prominent (Figure 4, *C*) but suffers from a nonspecific ablation (Figure 4, *F*), which is possibly due to heat dissipation from high water attenuation at 980 nm. Notably, the laser irradiance used in our study (15 W/cm^2) is lower than the previous reported irradiances on branched nanoparticles (38 W/cm^2), Au-Au_2S nanoshells (80 W/cm^2), hollow nanospheres (32 W/cm^2), and nanoshells (35 W/cm^2), but higher than irradiances on nanocubes (4 W/cm^2) and nanocages (1.5 W/cm^2).[14,17,18,22,25,26] However, this comparison is oversimplified. As mentioned above, the photothermal response depends on the many parameters including laser dosage, nanoparticles' plasmon resonance, and intracellular particle concentration.[2] Because nanoparticles' uptake varies between different cell lines and different nanoparticles in terms of concentration, shape, dispersity, and surface modification, it is practically impossible to make a fair comparison with different studies. It is beyond the scope of this article to address the uptake variation of different nanoparticles on different cell lines, or to compare the photothermal therapeutic efficacy of different aspherical nanoparticles.

The photothermal ablation in vivo was demonstrated using PEGylated nanostars examined through a dorsal window chamber on mice. Because of their strong TPL, nanostars allow short imaging-integration time and hence enable real-time particle tracking, which provides a convenient way to optically assess the particle distribution in vivo.[11] Within 1 hour following the injection, nanostars distributed mostly in the blood vessels, generating a clear vasculature pattern with minimal tissue autofluorescence background (Figure 5, *A*, *B*). On day 3 (~48 hours after injection), because vascular pattern was no longer clearly discernible, FITC-dextran was injected to visualize the vasculature (Figure 6, *B*, *C*). Although some nanostars remained in the perivascular space, many nanoparticles permeated beyond the perivascular space and into the deep tissue. Although the distribution of PEGylated nanostars is rather nonspecific in this study, we can control the extent of photothermal ablation by adjusting the area of irradiation.

After the irradiation, localized photothermal damage was observed both grossly (Figure 6, *D*) and microscopically (Figure 6, *E*, *F*) on the mouse receiving combined nanostars and laser treatment. Blood oozing after PTT indicated physical vascular damage; the blood clot remained in the chamber for a week until the mouse was euthanized. The occurrence of scarring later on the backside of the window chamber reflects the low attenuation of NIR laser in tissue. Bleeding, however, may not be favorable for solid-tumor treatment for fear of distant metastasis from spreading of tumor cells via the bloodstream. The extent of photothermal damage can be controlled by the laser dosage to reduce the unwanted side

effect. Microscopically, the PTT spot was filled with blood, FITC-dextran (massive green color), and nanostars (white color) (Figure 6, *E*, *F*). For the mouse injected with PEGylated nanospheres, vascular pattern could not be easily observed even under much higher laser power (20% transmission), whereas tissue autofluorescence became predominant (Supplementary Figure S4, *B*, *D*). After the laser irradiation, no gross physical damage was observed (Supplementary Figure S4, *A*, *C*). Note that even though the irradiance used in our study (1.1 W/cm^2) was higher than the maximum permissible exposure of skin (0.3 W/cm^2) for a 785-nm CW laser based on the ANSI regulation,[28] no apparent damage from laser alone was observed.

In this proof-of-concept study, we employed gold nanostars as an efficient photothermal transducer for hyperthermic therapy. Although surfactant-free nanostars are susceptible to aggregation, PEGylation can be applied to reduce the aggregation in physiological conditions. From simulation, the nanostar exhibits a high C_{abs}/C_{sca} ratio. In solution, nanostars with their plasmons matching the laser transduce photon energy efficiently to heat. In vitro, the photothermal ablation on cancer cells was only visible when both NIR laser irradiation and nanostars intracellular delivery were combined. In vivo, photothermal ablation was observed right at the laser spot on a dorsal window chamber from a mouse injected with PEGylated nanostars but not with PEGylated nanospheres. Further investigations will be performed to optimize the effectiveness of the PTT modality using nanostars.

Acknowledgments

This work was sponsored by the National Institutes of Health (grants R01 EB006201 and R01 ES014774) and the Department of Defense (W81XWH-09-1-0064).

References

1. Jain RK. Transport of molecules, particles, and cells in solid tumors. Annu Rev Biomed Eng. 1999; 1:241–63. [PubMed: 11701489]
2. Kennedy LC, Bickford LR, Lewinski NA, Coughlin AJ, Hu Y, Day ES, et al. A new era for cancer treatment: gold-nanoparticle-mediated thermal therapies. Small. 2011; 7:169–83. [PubMed: 21213377]
3. Boisselier E, Astruc D. Gold nanoparticles in nanomedicine: preparations, imaging, diagnostics, therapies and toxicity. Chem Soc Rev. 2009; 38:1759–82. [PubMed: 19587967]
4. Jain PK, Lee KS, El-Sayed IH, El-Sayed MA. Calculated absorption and scattering properties of gold nanoparticles of different size, shape, and composition: applications in biological imaging and biomedicine. J Phys Chem B. 2006; 110:7238–48. [PubMed: 16599493]
5. Sau TK, Rogach AL, Jackel F, Klar TA, Feldmann J. Properties and applications of colloidal nonspherical noble metal nanoparticles. Adv Mater. 2010; 22:1805–25. [PubMed: 20512954]
6. Weissleder R. A clearer vision for in vivo imaging. Nat Biotechnol. 2001; 19:316–7. [PubMed: 11283581]
7. Xia Y, Li W, Cobley CM, Chen J, Xia X, Zhang Q, et al. Gold nanocages: from synthesis to theranostic applications. Acc Chem Res. 2011; 44:914–24. [PubMed: 21528889]
8. Zhang J. Biomedical applications of shape-controlled plasmonic nanostructures: a case study of hollow gold nanospheres for photothermal ablation therapy of cancer. J Phys Chem Lett. 2010; 1:686–95.
9. Huang X, El-Sayed IH, Qian W, El-Sayed MA. Cancer cell imaging and photothermal therapy in the near-infrared region by using gold nanorods. J Am Chem Soc. 2006; 128:2115–20. [PubMed: 16464114]
10. Tong L, Wei Q, Wei A, Cheng JX. Gold nanorods as contrast agents for biological imaging: optical properties, surface conjugation and photothermal effects. Photochem Photobiol. 2009; 85:21–32. [PubMed: 19161395]

11. Yuan H, Khoury CG, Hwang H, Wilson CM, Grant GA, Vo-Dinh T. Gold nanostars: surfactant-free synthesis, 3D modelling, and two-photon photoluminescence imaging. Nanotechnology. 2012; 075102:23.
12. Au L, Zhang Q, Cobley CM, Gidding M, Schwartz AG, Chen J, et al. Quantifying the cellular uptake of antibody-conjugated au nanocages by two-photon microscopy and inductively coupled plasma mass spectrometry. ACS Nano. 2010; 4:35–42. [PubMed: 19954236]
13. Dewhirst MW, Vujaskovic Z, Jones E, Thrall D. Re-setting the biologic rationale for thermal therapy. Int J Hyperthermia. 2005; 21:779–90. [PubMed: 16338861]
14. Van de Broek B, Devoogdt N, D'Hollander A, Gijs HL, Jans K, Lagae L, et al. Specific cell targeting with nanobody conjugated branched gold nanoparticles for photothermal therapy. ACS Nano. 2011; 5:4319–28. [PubMed: 21609027]
15. Choi WI, Kim JY, Kang C, Byeon CC, Kim YH, Tae G. Tumor regression in vivo by photothermal therapy based on gold-nanorod-loaded, functional nanocarriers. ACS Nano. 2011; 5:1995–2003. [PubMed: 21344891]
16. Yi DK, Sun IC, Ryu JH, Koo H, Park CW, Youn IC, et al. Matrix metalloproteinase sensitive gold nanorod for simultaneous bioimaging and photothermal therapy of cancer. Bioconjug Chem. 2010; 21:2173–7. [PubMed: 21062090]
17. Wu X, Ming T, Wang X, Wang P, Wang J, Chen J. High-photoluminescence-yield gold nanocubes: for cell imaging and photothermal therapy. ACS Nano. 2010; 4:113–20. [PubMed: 20014823]
18. Gobin AM, Watkins EM, Quevedo E, Colvin VL, West JL. Near-infrared-resonant gold/gold sulfide nanoparticles as a photothermal cancer therapeutic agent. Small. 2010; 6:745–52. [PubMed: 20183810]
19. von Maltzahn G, Park JH, Agrawal A, Bandaru NK, Das SK, Sailor MJ, et al. Computationally guided photothermal tumor therapy using long-circulating gold nanorod antennas. Cancer Res. 2009; 69:3892–900. [PubMed: 19366797]
20. Huff TB, Tong L, Zhao Y, Hansen MN, Cheng JX, Wei A. Hyperthermic effects of gold nanorods on tumor cells. Nanomedicine (Lond). 2007; 2:125–32. [PubMed: 17716198]
21. Huang X, Peng X, Wang Y, Wang Y, Shin DM, El-Sayed MA, et al. A reexamination of active and passive tumor targeting by using rod-shaped gold nanocrystals and covalently conjugated peptide ligands. ACS Nano. 2010; 4:5887–96. [PubMed: 20863096]
22. Hirsch LR, Gobin AM, Lowery AR, Tam F, Drezek RA, Halas NJ, et al. Metal nanoshells. Ann Biomed Eng. 2006; 34:15–22. [PubMed: 16528617]
23. Dickerson EB, Dreaden EC, Huang X, El-Sayed IH, Chu H, et al. Gold nanorod assisted near-infrared plasmonic photothermal therapy (PPTT) of squamous cell carcinoma in mice. Cancer Lett. 2008; 269:57–66. [PubMed: 18541363]
24. Jang B, Park JY, Tung CH, Kim IH, Choi Y. Gold nanorod-photosensitizer complex for near-infrared fluorescence imaging and photodynamic/photothermal therapy in vivo. ACS Nano. 2011; 5:1086–94. [PubMed: 21244012]
25. Chen J, Wiley B, Li Z, Campbell D, Saeki F, Cang H, et al. Gold nanocages: engineering their structure for biomedical applications. Adv Mater. 2005; 17:2255–61.
26. Lu W, Xiong C, Zhang G, Huang Q, Zhang R, Zhang JZ, et al. Targeted photothermal ablation of murine melanomas with melanocyte-stimulating hormone analog-conjugated hollow gold nanospheres. Clin Cancer Res. 2009; 15:876–86. [PubMed: 19188158]
27. Chen J, Glaus C, Laforest R, Zhang Q, Yang M, Gidding M, et al. Gold nanocages as photothermal transducers for cancer treatment. Small. 2010; 6:811–7. [PubMed: 20225187]
28. American National Standards Institute. American National Standard for safe use of lasers. Orlando (Fla): Laser Institute of America; 2000.
29. Vo-Dinh T, Hiromoto M, Begun G, Moody R. Surface-enhanced Raman spectrometry for trace organic analysis. Anal Chem. 1984; 56:1667–70.
30. Vo-Dinh T. Surface-enhanced Raman spectroscopy using metallic nanostructures. Trends Anal Chem. 1998; 17:557–82.
31. Yan F, Vo-Dinh T. Surface-enhanced Raman scattering detection of chemical and biological agents using a portable Raman integrated tunable sensor. Sens Actuators B. 2007; 121:61–6.

32. Khoury CG, Vo-Dinh T. Gold nanostars for surface-enhanced Raman scattering: synthesis, characterization and optimization. J Phys Chem C. 2008; 112:18849–59.
33. Fales AM, Yuan H, Vo-Dinh T. Silica-coated gold nanostars for combined surface-enhanced Raman scattering (SERS) detection and singletoxygen generation: a potential nanoplatform for theranostics. Langmuir. 2011; 27:12186–90. [PubMed: 21859159]
34. Hrelescu C, Sau TK, Rogach AL, Jackel F, Feldmann J. Single gold nanostars enhance Raman scattering. Appl Phys Lett. 2009; 153113:94.
35. Nalbant Esenturk E, Hight Walker A. Surface-enhanced Raman scattering spectroscopy via gold nanostars. J Raman Spectrosc. 2009; 40:86–91.
36. Guerrero-Martínez A, Barbosa S, Pastoriza-Santos I, Liz-Marzán LM. Nanostars shine bright for you. Curr Opin Colloid Interface Sci. 2011; 16:118–27.
37. Schütz M, Steinigeweg D, Salehi M, Kömpe K, Schlücker S. Hydrophilically stabilized gold nanostars as SERS labels for tissue imaging of the tumor suppressor p63 by immuno-SERS microscopy. Chem Comm. 2011; 47:4216–8. [PubMed: 21359379]
38. Kim C, Song HM, Cai X, Yao J, Wei A, Wang LV. In vivo photoacoustic mapping of lymphatic systems with plasmon-resonant nanostars. J Mater Chem. 2011; 21:2841–4. [PubMed: 21660122]
39. Dondapati SK, Sau TK, Hrelescu C, Klar TA, Stefani FD, Feldmann J. Label-free biosensing based on single gold nanostars as plasmonic transducers. ACS Nano. 2010; 4:6318–22. [PubMed: 20942444]
40. Song HM, Wei Q, Ong QK, Wei A. Plasmon-resonant nanoparticles and nanostars with magnetic cores: synthesis and magnetomotive imaging. ACS Nano. 2010; 4:5163–73. [PubMed: 20690598]
41. Johnson PB, Christy RW. Optical constants of the noble metals. Phys Rev B. 1972; 6:4370–9.
42. Chen H, Shao L, Ming T, Sun Z, Zhao C, Yang B, et al. Understanding the photothermal conversion efficiency of gold nanocrystals. Small. 2010; 6:2272–80. [PubMed: 20827680]
43. Baffou G, Quidant R, Girard C. Heat generation in plasmonic nanostructures: influence of morphology. Appl Phys Lett. 2009; 153109:94.
44. Rodríguez-Oliveros R, Sánchez-Gil JA. Gold nanostars as thermoplasmonic nanoparticles for optical heating. Opt Express. 2012; 20:621–6. [PubMed: 22274385]
45. Lévy R, Shaheen U, Cesbron Y. Gold nanoparticles delivery in mammalian live cells: a critical review. Nano Rev. 2010; 1:4889.
46. Hu L, Mao Z, Gao C. Colloidal particles for cellular uptake and delivery. J Mater Chem. 2009; 19:3108–15.
47. Hutter E, Boridy S, Labrecque S, Lalancette-Hébert M, Kriz J, Winnik FM, et al. Microglial response to gold nanoparticles. ACS Nano. 2010; 4:2595–606. [PubMed: 20329742]
48. Dobrovolskaia MA, Patri AK, Zheng J, Clogston JD, Ayub N, Aggarwal P, et al. Interaction of colloidal gold nanoparticles with human blood: effects on particle size and analysis of plasma protein binding profiles. Nanomed Nanotechnol Biol Med. 2009; 5:106–17.
49. Chithrani DB. Intracellular uptake, transport, and processing of gold nanostructures. Mol Membr Biol. 2010; 27:299–311. [PubMed: 20929337]
50. Iversen TG, Skotland T, Sandvig K. Endocytosis and intracellular transport of nanoparticles: present knowledge and need for future studies. Nano Today. 2011; 6:176–85.

Appendix. Supplementary data

Supplementary data to this article can be found online at doi:10.1016/j.nano.2012.02.005.

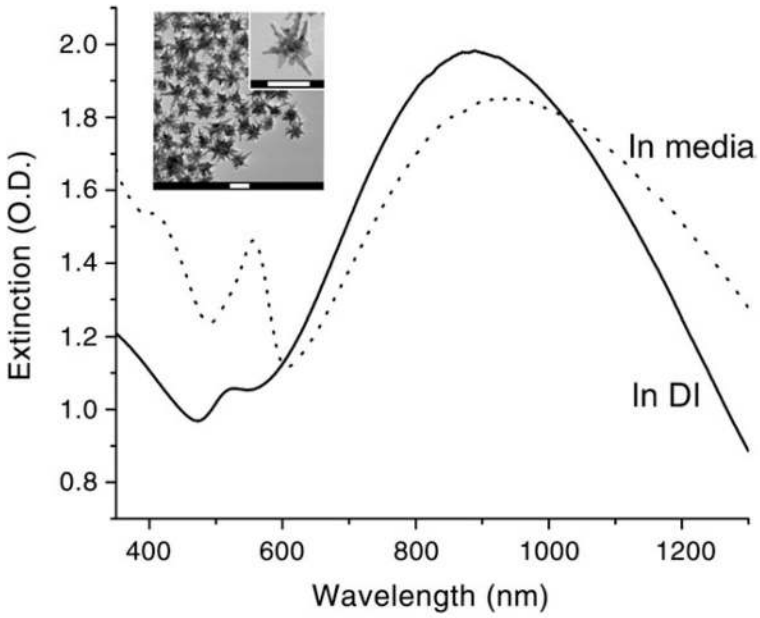

Figure 1.

The extinction spectra of 0.2 nM nanostars used for in vitro PTT. In deionized water (DI; *solid line*) the plasmon peaks at around 890 nm with a small peak around 525 nm. In FBS-containing growth medium (*dotted line*), the nanostars' plasmon peak red-shifted and intensity decreased. The phenol red signal from the growth medium was observed around 560 nm. TEM image of nanostars (*inset*). Scale bars, 50 nm.

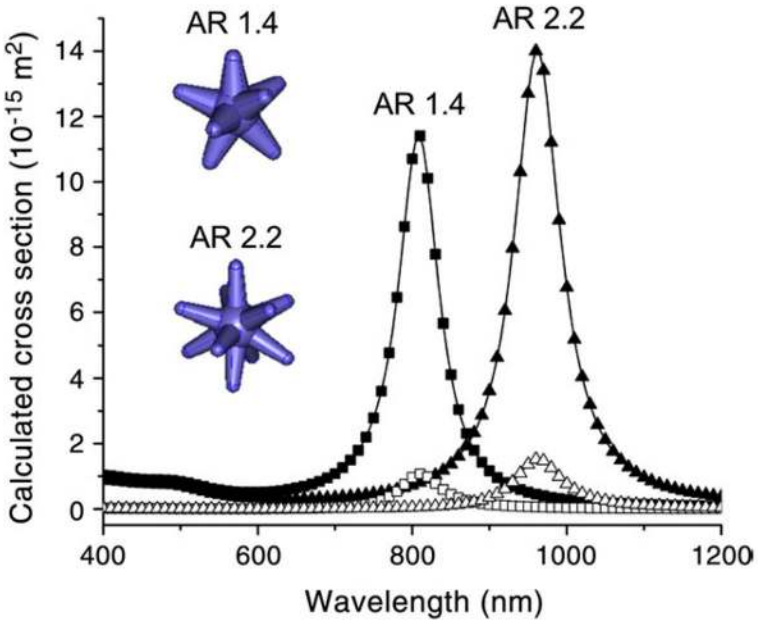

Figure 2.

The simulated spectra (*splined*) of absorption (*solid symbols*) and scattering (*open symbols*) cross-sections of nanostars of two different aspect ratios (ARs; branch length/branch base width) (*inset*). The 3D models of two nanostars are simulated. The geometry data used for simulation are listed below. AR 1.4: core 24 nm; branch length/branch base width 19/13.5 nm; branch number 8. AR 2.2: core 22 nm, branch length/branch base width 22/10 nm; branch number 10.[11]

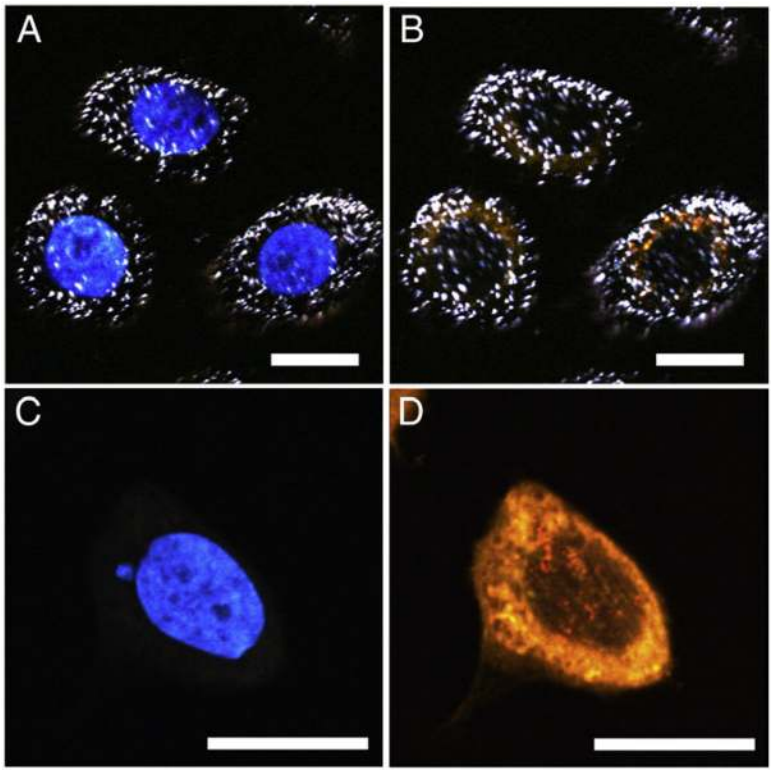

Figure 3.
Multiphoton microscopy images of SKBR3 cells incubated with nanostars (*top*) and medium alone (*bottom*), imaged under 750 nm **(A**, **C)** and 850 nm **(B**, **D)** excitation. Nanostars (*white dots*) appeared mostly in the cytoplasm. Nucleus and cytoplasm were stained blue and orange using Hoechst 33342 and FM 1-43 FX, respectively. Scale bars, 20 μm.

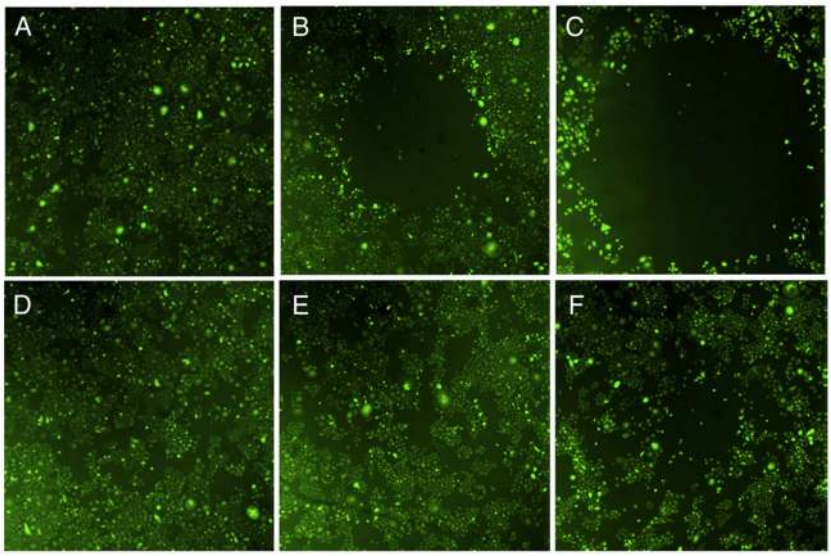

Figure 4.

Fluorescence images of viable SKBR3 cells after the laser treatment. Viable cells appear green by converting nonfluorescing dye into green fluorescence. Empty area indicates successful photothermal ablation. Cells were incubated 1 hour with 0.2 nM nanostars (*top*) and medium alone (*bottom*) before the irradiation. Laser irradiation (980 nm, 15 W/cm^2) was applied for 1 minute **(A**, **D)**, 3 minutes **(B**, **E)**, and 5 minutes **(C**, **F)**. Image sizes are 3 × 3 mm^2.

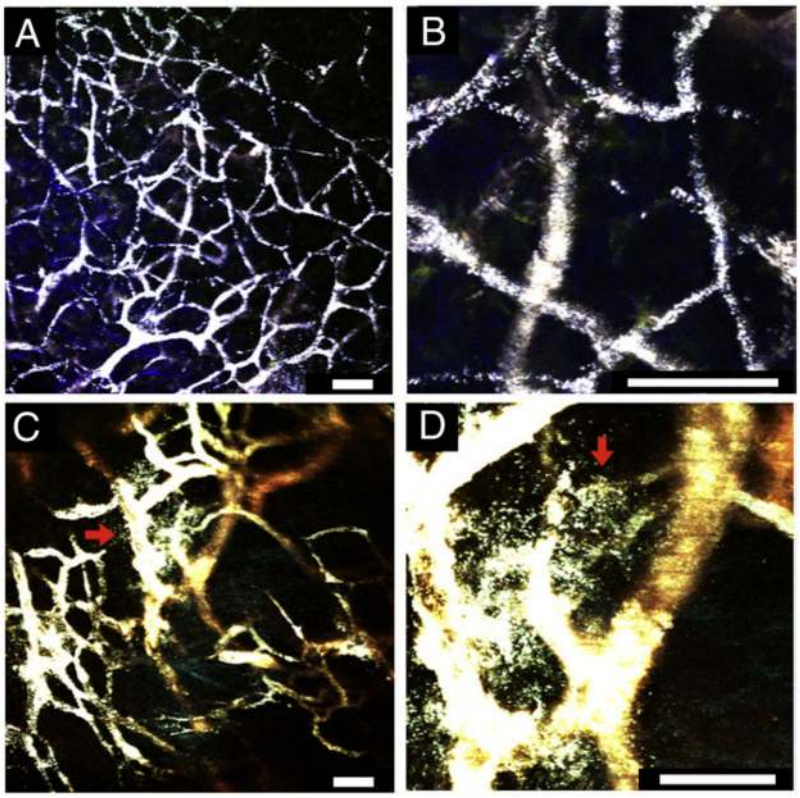

Figure 5.

Multiphoton microscopy imaging through a dorsal window chamber 30 minutes following the systemic injection of PEGylated nanostars (50 nM, 50 μL). A clear vasculature pattern, delineated by the intravascular nanostars, is visible with minimal tissue autofluorescence under 3% transmission power **(A)**; zoom-in **(B)**. In some regions, extravasation of nanostars (numerous white dots outside the vessel; *red arrows*) is observed **(C)**; zoom-in **(D)**. Scale bars, 50 μm.

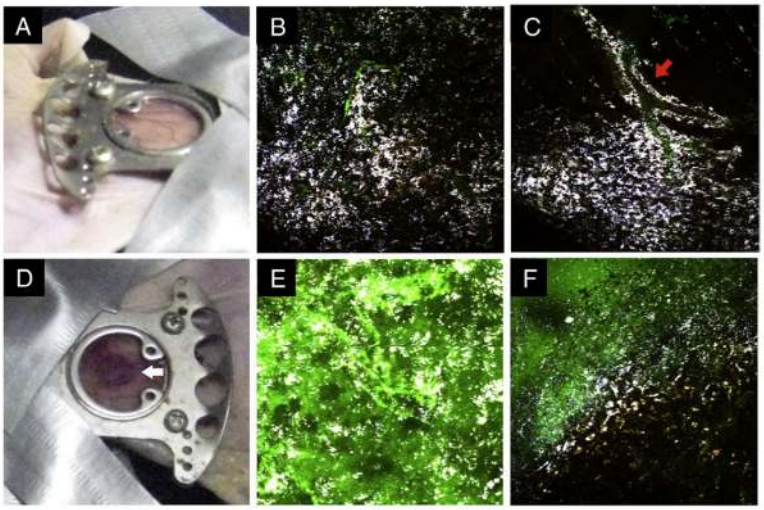

Figure 6.

Photographs and multiphoton microscopy images 48 hours after nanostars infusion before (*top*) and after (*bottom*) the laser treatment. Before the irradiation, the window appeared intact and uninflamed **(A)**. Nanostars (*white color*) scattered in the tissue **(B)** with some remaining near the perivascular space **(C**; *red arrow*). Green color from FITC-dextran delineates the blood vessels. After the laser irradiation (785 nm 1.1 W/cm^2, 10 minutes), a localized oozing of blood became visible **(D**; *white arrow*). Nanostars distributed more randomly or into clusters. Leakage of FITC-dextran into the tissue was apparent in the irradiated spot **(E)** but not outside the spot **(F)**. Microscope images are 508 × 508 μm^2 and taken under 850-nm 3% transmission power.

Table 1

The absorption and scattering cross-section coefficients of aspherical AuNPs

	C_{abs} ($\times 10^{-15}$ m^2)	C_{sca} ($\times 10^{-15}$)	C_{abs}/C_{sca}	Reference
Nanorods, width/length: 17.9/69.8 nm, at 820 nm	14.9	4.2	3.55	4
Nanoshells, R_1/R_2: 60/70 nm, at 892 nm	50.9	32.5	1.57	4
Nanocages, edge length: 30 nm, at 825 nm	7.3	0.8	9.1	25
Au-Au_2S nanoshell, R_1/R_2: 21/25 nm, at 800 nm	3.2	0.16	20.2	18
Nanostars, tip-to-tip: 66 nm, AR: 2.2, at 960 nm	14.0	1.52	9.2	This work
Nanostars, tip-to-tip: 62 nm, AR: 1.4, at 810 nm	11.4	1.06	10.8	This work

Abbreviation: AR, aspect ratio.

The values of each simulated C_{abs} and C_{sca} were obtained at their plasmon peak wavelengths.